Self-propelled plate in wakes behind tandem cylinders

Wenjiang Wang, Haibo Huang,* and Xi-Yun Lu
Department of Modern Mechanics, University of Science and Technology of China, Hefei, Anhui 230026, China

(Received 29 March 2019; published 20 September 2019)

Fish may take advantage of environmental vortices to save the cost of locomotion. The complex hydrodynamics shed from multiple physical objects may significantly affect fish refuging (holding stationary). Taking a model of a self-propelled flapping plate, we numerically studied the locomotion of the plate in wakes of two tandem cylinders. In most simulations, the plate heaves at its initial position G_0 before the flow comes (releasing Style I). In the typical wake patterns, the plate may hold stationary, drift upstream, or drift downstream. The phase diagrams of these modes in the G_0-A plane for the vortex shedding patterns were obtained, where A is the flapping amplitude. It is observed that the plate is able to hold stationary at multiple equilibrium locations after it is released. Meanwhile, the minimum amplitude and the input power required for the plate seem inversely proportional to the shedding vortex strength. The effect of releasing style was also investigated. If the plate keeps stationary and does not flap until the vortex shedding is fully developed (releasing Style II), then the plate is able to hold stationary at some equilibrium locations but the flapping plate has a very minor effect on the shedding vortices. However, in Style I, the released plate is able to achieve more equilibrium locations through adjusting the phase of vortex shedding. The effort of the preflapping in Style I is not in vain, because although it consumes more energy, it becomes easier to hold stationary later. The relevant mechanism is explored.

DOI: 10.1103/PhysRevE.100.033114

I. INTRODUCTION

The surroundings of swimming fish are always unpredictable when they seek refuge. When fish swim in a fluid, the motion of each fish may be influenced by others or physical structures through the flow-mediated interaction among them. Swimming fish may encounter unsteady wakes generated by stationary objects or the schooling behavior. Fish schooling has been extensively studied for many years [1,2]. Besides the social and sensory factors, the hydrodynamic mechanism is an essential factor which may promote swimming efficiency. Fish in schools are supposed to obtain a hydrodynamic advantage by placing themselves in appropriate locations in the wake of other swimmers. They may reduce the cost of locomotion by taking advantage of the wakes shed by neighbors within the school [3–6].

However, little biological evidence of hydrodynamic advantage in the appropriate position patterns has been found [2]. Abrahams and Colgan [7] pointed out the controversy may be derived from ignoring the potential trade-offs involved in school functions. Due to the difficulty of experimental measurement on the energetic savings of schooling, only limited experimental evidences [6,8,9] have shown that the individuals can obtain a hydrodynamic advantage from the collective locomotion. Hence, whether there is a hydrodynamic benefit experienced by biological propulsors in the school is still an open question. Nowadays, more attentions were paid to the swimming fish in the wake. Alben [10] formulated a theoretical model for the swimming of a flexible body in a vortex and got the relationship between the body shape and resulting efficiency. Recently self-propulsion models are used to investigate this issue [11–13]. In the simulations and experiments, the spacing between flapping plates is not fixed but dynamically selected as a result of flow-mediated coupling between the wings, which is close to the real situation. The studies have shown that in the emergent configurations, the follower may take advantage from the upstream shedding vortices. In these studies, the shedding vortices encountered by the following swimmers are reverse Kármán vortices.

Here we focus on whether the swimmer is able to hold stationary in the Kármán vortex street instead of the reverse Kármán vortex street, which is the situation of fish refuging behind stationary physical structures. Previous studies have shown that fishes often prefer to exploit turbulence associated with physical structures to reduce locomotory costs [14–16]. Fishes may detect these vortices by their lateral line systems and acquire energy from the fluid by bending their bodies to synchronize with the vortices. The wake behind simple geometric objects in a moving fluid has been well characterized by fluid mechanists. Different Kármán vortex shedding modes represent different consistent flow perturbations.

It is noticed that there have been some studies on the interactions between the cylinder and fishlike undulating foil or flexible plate, but they are not self-propelled cases [17–20]. In the literature, very few studies on the flow-mediated interactions between the physical structures and self-propelled flexible plate have been carried out. As far as we know, the only relevant numerical study was conducted by Park *et al.* [21], in which a self-propelled flexible fin is in the wake of a circular cylinder at a fixed Reynolds number $\mathrm{Re} = 200$. The self-propulsion is induced by the prescribed heave motion at the leading edge of the fin but whose longitudinal swimming is free. It is shown that the fin is able to hold stationary position spontaneously with the help of the vortex street behind the cylinder. A slaloming behavior between the vortex cores

*huanghb@ustc.edu.cn

 ©2019 American Physical Society

was observed when the fin flaps at the equilibrium position. However, the wake behind the single cylinder at a fixed Re may be too simple.

By altering the dimensions of a given object, Liao *et al*. [22] systematically investigated the effect of vortical flows behind the object on swimming fish. They observed the Kármán gaits over a range of flow velocities and cylinder diameters. The Kármán gait is a unique swimming style that fish refuging behind the cylinder adopt. In the Kármán gait, the body exhibits a low frequency lateral motions with a much larger amplitude than that in the steady swimming. They found that Kármán gait offers almost 50% energy savings for the fish as it reduces the muscle activity and oxygen consumption required to swim against a current [23,24]. Beal *et al*. [25] found even anesthetized trout may maintain motion in the vortex street behind the *D*-shaped cylinder. It qualitatively suggests that a dead fish may be able to extract energy from the vortex street to produce a thrust.

Recently to initiate a better understanding of how fish refuge in more complex hydrodynamic environments, Stewart *et al*. [26] characterized the interaction between fish and the wake behind two tandem cylinders. The experimental results showed that increasing gap spacing of the cylinders (D_x) decreased the strength of the vortex street and the frequency of the vortex shedding by approximately 53% and 20% for all speeds, respectively. Trout were found able to Kármán gait behind all cylinder arrangements in their study. However, they Kármán gaited over twice as often behind closely spaced cylinders ($\frac{D_x}{D} = 0.7$, 1.1, and 1.5, D is the cylinder diameter). Their computational fluid dynamics simulations showed that widely spaced cylinders produce weaker, more widely spaced and less-organized vortices, which discouraged Kármán gait [26]. However, in the computational fluid dynamics simulations, there are only two cylinders without any self-propulsion object. How the vortex shedding affects the Kármán gait is still unknown. Therefore, further numerical investigation including a self-propulsion model is necessary because numerical simulations are able to present more details and relevant quantitative information, which may be difficult to obtain in experiments.

In the present study, we carried out numerical simulations on the locomotion of a self-propelled flexible plate in a complicated vortical environment, which is generated by two tandem cylinders. The purpose of this study is to explore the fundamental mechanisms why the self-propelled flexible plate is able to hold stationary in the wake of tandem cylinders.

The remainder of the paper is organized as follows: The physical problem and mathematical formulation are presented in Sec. II. The numerical method and validation are described in Sec. III. Results are discussed in Sec. IV. and concluding remarks are addressed in Sec. V.

II. PHYSICAL PROBLEM AND MATHEMATICAL FORMULATION

We consider a uniform viscous flow passing two tandem circular cylinders with diameter D and a flexible plate with length L. The plate is introduced behind the downstream cylinder. The schematic diagram is shown in Fig. 1. Two tandem cylinders are stationary and fixed with a gap spacing

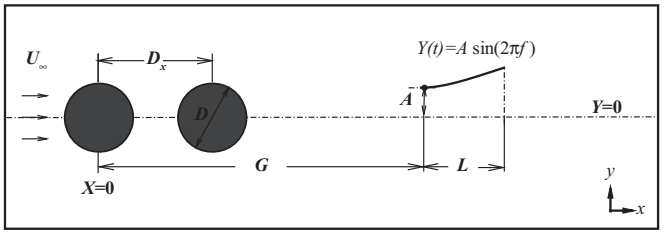

FIG. 1. Schematic diagram of a self-propelled flexible plate behind two tandem cylinders.

D_x and the Kármán vortex street may be generated in the wake. The gap spacing between the flexible plate and the upstream cylinder center in the horizontal direction is G. If not specified, the flexible plate is kept flapping and released until the vortical structures are fully developed. The leading-edge of the plate is forced to heave sinusoidally with amplitude A and frequency f laterally. Similar to the treatment of the previous studies [13,27], the forced motion of the leading-edge is described by

$$y(t) = A\sin(2\pi f t). \tag{1}$$

Meanwhile, the plate is unconstrained in the horizontal direction. It hints that only the leading-edge of plate is restricted with the prescribed lateral heaving motion and due to the deformation of the plate, the fluid-plate interaction drives its longitudinal swimming. Here, a Lagrangian coordinate s along the plate surface is defined to describe the configuration and motion of the plate. The fluid flow is governed by the viscous incompressible Navier-Stokes equations

$$\frac{\partial \boldsymbol{v}}{\partial t} + \boldsymbol{v}\cdot\nabla\boldsymbol{v} = -\frac{1}{\rho}\nabla p + \frac{\mu}{\rho}\nabla^2\boldsymbol{v} + \boldsymbol{f}, \tag{2}$$

$$\nabla\cdot\boldsymbol{v} = 0, \tag{3}$$

where $\boldsymbol{v}$ is the velocity, p is the pressure, ρ is the density of the fluid, μ is the dynamic viscosity, and $\boldsymbol{f}$ is the Eulerian momentum force acting on the surrounding fluid due to the immersed boundary, as constrained by the no-slip boundary condition. The structural equation is employed to describe the deformation and motion of plate [28],

$$\rho_s h\frac{\partial^2\boldsymbol{X}}{\partial t^2} - Eh\frac{\partial}{\partial s}\left\{\left[1-\left(\frac{\partial\boldsymbol{X}}{\partial s}\cdot\frac{\partial\boldsymbol{X}}{\partial s}\right)^{-1/2}\right]\frac{\partial\boldsymbol{X}}{\partial s}\right\} + EI\frac{\partial^4\boldsymbol{X}}{\partial s^4} = \boldsymbol{F}_s, \tag{4}$$

where s is the Lagrangian coordinate along the plate, $\boldsymbol{X} = (X, Y)$ is the position vector of the plate, $\boldsymbol{F}_s$ is the Lagrangian force exerted on the plate by the fluid, and ρ_s is the structural linear mass density of the plate. Eh and EI denote the structural stretching rigidity and bending rigidity, respectively. At the leading-edge of the plate, the clamped boundary condition is adopted, i.e.,

$$-Eh\left(1-\left|\frac{\partial\boldsymbol{X}}{\partial s}\right|^{-1}\right)\frac{\partial\boldsymbol{X}}{\partial s} + EI\frac{\partial^3\boldsymbol{X}}{\partial^3 s} = 0, \quad Y(t) = y(t),$$

$$\frac{\partial\boldsymbol{X}}{\partial s} = (1, 0). \tag{5}$$

At the free end of the plate, the boundary condition is expressed as

$$-Eh\left(1-\left|\frac{\partial \boldsymbol{X}}{\partial s}\right|^{-1}\right)\frac{\partial \boldsymbol{X}}{\partial s}+EI\frac{\partial^3 \boldsymbol{X}}{\partial^3 s}=0,\quad \frac{\partial^2 \boldsymbol{X}}{\partial s^2}=0. \tag{6}$$

Moreover, $\boldsymbol{X}(s,0)=[s,y(0)]$, $\dot{\boldsymbol{X}}(s,0)=(0,0)$ is the initial condition for the plate.

We choose the far-field velocity $U=U_\infty$, the cylinder diameter D, the fluid density ρ as characteristic quantities to normalize the above equation. Based on the nondimensional analysis, there are several dimensionless parameters in our problem: the Reynolds number $\mathrm{Re}=\rho UD/\mu$, the stretching stiffness $S=Eh/\rho U^2D$, the bending stiffness $K=EI/\rho U^2D^3$, the mass ratio of the plate and the fluid $M=\rho_s h/\rho D$, the heaving amplitude A/D, the distance of two tandem cylinder center D_x/D, the horizontal gap between the flexible plate and the upstream cylinder center G/D. In the following descriptions, A, D_x, and G are used to represent the normalized quantities A/D, D_x/D, and G/D, respectively. It should be noted that we set $t=0$ as the releasing moment.

III. NUMERICAL METHOD AND VALIDATION

A. Numerical method

The governing equations of the fluid-plate problem are solved numerically by an immersed boundary-lattice Boltzmann method for the fluid flow [29] and a finite element method for the motion of the flexible plates [30]. The immersed boundary (IB) method has been extensively applied to problems involving moving boundaries immersed in a viscous fluid flow [31,32]. When the IB method is used to treat flow-structure interaction, the Lagrangian interaction force $\boldsymbol{F}_s$ in Eq. (4) between the fluid and the immersed boundary can be calculated by the feedback law [31,32]:

$$\begin{aligned}\boldsymbol{F}_s(s,t)=\alpha\int_0^t[\boldsymbol{V}_f(s,t')-\boldsymbol{V}_s(s,t')]dt'\\+\beta[\boldsymbol{V}_f(s,t)-\boldsymbol{V}_s(s,t)].\end{aligned} \tag{7}$$

The parameters α and β are large positive free constants ($\alpha=10^3$ and $\beta=1$) to enforce the no-slip condition, $\boldsymbol{V}_s=\frac{\partial \boldsymbol{X}}{\partial t}$ is the plate velocity and $\boldsymbol{V}_f$ is the fluid velocity at the position of the body obtained by interpolation:

$$\boldsymbol{V}_f(s,t)=\int \boldsymbol{v}(x,t)\delta[\boldsymbol{x}-\boldsymbol{X}(s,t)]d\boldsymbol{x}. \tag{8}$$

In the IB scheme, the body force term $\boldsymbol{f}$ in Eq. (2) is used as an interaction force between the fluid and the immersed boundary to enforce the no-slip velocity boundary condition. The body force $\boldsymbol{f}$ on the Eulerian points can be obtained from the Lagrangian force $\boldsymbol{F}_s$ using the Dirac δ function [31], i.e.,

$$\boldsymbol{f}(x,t)=-\int \boldsymbol{F}_s(x,t)\delta[\boldsymbol{x}-\boldsymbol{X}(s,t)]ds. \tag{9}$$

In this study, a four-point regularized δ function is used,

$$\delta_h=\frac{1}{\Delta x\Delta y}\phi\left(\frac{x}{\Delta x}\right)\phi\left(\frac{y}{\Delta y}\right), \tag{10}$$

$$\phi(r)=\begin{cases}(3-2|r|+\sqrt{1+4|r|-4r^2})/8, & |r|<1,\\ (5-2|r|-\sqrt{-7+12|r|-4r^2})/8, & 1\leqslant|r|<2,\\ 0, & |r|\geqslant 2,\end{cases} \tag{11}$$

where $|r|$ is the distance between the Lagrangian point and the nearby Eulerian grid points.

Furthermore, the lattice Boltzmann equation (LBE) has been widely used to simulate complex flows as an alternative to conventional numerical methods for the Navier-Stokes equations [29,33–36]. The LBE with the BGK model is

$$\begin{aligned}&f_i(\boldsymbol{x}+\boldsymbol{e}_i\Delta t,t+\Delta t)-f_i(\boldsymbol{x},t)\\&=-\frac{1}{\tau}\left[f_i(\boldsymbol{x},t)-f_i^{\mathrm{eq}}(\boldsymbol{x},t)\right]+\Delta t F_i,\end{aligned} \tag{12}$$

where τ is the nondimensional relaxation time related to fluid viscosity, Δt is the time step, and $f_i(\boldsymbol{x},t)$ is the distribution function associated with discrete particle velocity $\boldsymbol{e}_i$. The equilibrium distribution function f_i^{eq} and the forcing term F_i [33] are defined as

$$f_i^{\mathrm{eq}}=\omega_i\rho\left[1+\frac{\boldsymbol{e}_i\cdot\boldsymbol{v}}{c_s^2}+\frac{\boldsymbol{v}\boldsymbol{v}:(\boldsymbol{e}_i\boldsymbol{e}_i-c_s^2\boldsymbol{I})}{2c_s^4}\right], \tag{13}$$

$$F_i=\left(1-\frac{1}{2\tau}\right)\omega_i\left[\frac{\boldsymbol{e}_i-\boldsymbol{v}}{c_s^2}+\frac{\boldsymbol{e}_i\cdot\boldsymbol{v}}{c_s^4}\boldsymbol{e}_i\right]\cdot\boldsymbol{f}, \tag{14}$$

where ω_i is the weighting factor and c_s is the sound speed. The macrovariables velocity $\boldsymbol{v}$ and mass density ρ can be obtained through the distribution functions,

$$\rho=\sum_i f_i,\quad \rho\boldsymbol{v}=\sum_i \boldsymbol{e}_i f_i+\frac{1}{2}\boldsymbol{f}\Delta t. \tag{15}$$

Equation (4) for the deformable plate is discretized by a finite element method, and the deformation with large-displacement of the plate is handled by the corotational scheme [30]. A detailed description of the numerical method can be found in our previous papers [13,36]. Based on our careful examinations and validations shown below, the computational domain for the fluid flow is chosen as $-10\leqslant x\leqslant 40$ and $-10\leqslant y\leqslant 10$, which is large enough so that the blocking effects of the boundaries are not significant. The boundary condition $\boldsymbol{v}=(U,0)$ is used on the inlet, top, and bottom boundaries, where U represents the free-stream velocity, $\partial\boldsymbol{v}/\partial x=0$ on the outlet. At the initial time, the fluid velocity field is $\boldsymbol{v}=(U,0)$ in the entire computational domain. In the x and y direction the mesh is uniform with spacing $\Delta x=\Delta y=0.02$. The time step is $\Delta t=0.001$ for the simulations of fluid flow and plate deformation, with $T=1/f$ being the flapping period.

B. Validation

To validate the numerical method used in the present study, two typical cases are considered here. First, the flow passing a cylinder was simulated. The parameters in the simulation were identical to that in Park *et al*. [21]. The key parameters are

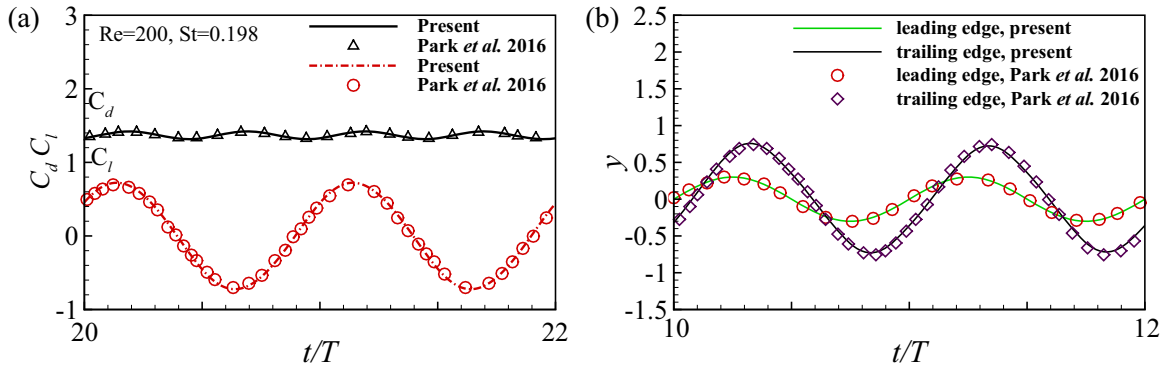

FIG. 2. (a) Time histories of the drag and lift coefficients of the cylinder without the flexible plate and (b) the locomotion of the leading-edge and trailing-edge of the flapping plate in the y direction as functions of time in the wake of a cylinder.

Re = 200 and Strouhal number St = 0.198. Figure 2(a) shows the time-dependent drag and lift coefficients of the cylinder without a flexible plate in the wake. It is seen that both the drag and lift coefficients are consistent with those in Park *et al*. [21]. Second, the flexible plate was "inserted" into the wake of the cylinder with the heaving amplitude $A = 0.3$ and frequency $f = 0.2$. After the plate reaching an equilibrium state, we plotted the trajectories of the leading and trailing edges of the plate (see Fig. 2). From Fig. 2(b), it is seen that the trajectories agree well with those in Park *et al*. [21].

The gird independence and time step independence studies were also performed. A typical case of a flexible plate flapping behind the wake of two tandem cylinders was simulated. In the case, the parameters were $D_x = 1.1$, $G_0 = 10$, $A = 0.3$, $f = 0.185$, $K = 0.5$, and Re = 200. The streamwise forces on the plate in simulations with different mesh size and time step size were shown in Fig. 3. It is seen that $\Delta x/L = 0.02$ and $\Delta t = 0.001$ are sufficient to achieve accurate results. Here, in all our simulations, $\Delta x/L = 0.02$ and $\Delta t = 0.001$ were adopted.

In addition, the numerical strategy used in this study has been validated and successfully applied to a wide range of flows, such as the interaction between a flexible filament and a downstream rigid body [20], the self-propulsion of a flapping flexible plate near the ground [36], and the collective locomotion of two closely spaced self-propelled flapping plates [13].

IV. RESULTS AND DISCUSSION

A. The patterns of vortex shedding around tandem cylinders

Tandem cylinders in a flow may shed more complex vortical structure than that of a single cylinder. Reviewing the vortical structure in the wake is the first step to understanding the mechanisms that affect the refuging behavior of fishes behind multiple objects.

In the literature [37–39], the flow patterns were classified into three distinct categories according to the flow structure, the vortex shedding frequency and the forces acting on the cylinders for Re > 100. The three flow patterns are single bluff-body (SBB), shear layer reattachment (SLR) and synchronization of vortex shedding (SVS). Their vortical structures are shown in Figs. 4(a)–4(c).

In the SBB pattern, two cylinders are closely-spaced and behave hydrodynamically as a single bluff body [see Fig. 4(a)]. The SLR pattern occurs at moderate spacings. The shear layers separating from the upstream cylinder reattach to the surface of the downstream one [see Fig. 4(b)]. In the SVS flow pattern, the large gap spacing allows both the cylinders to shed vortices at the same frequency. These vortices interact to form the downstream wake [see Fig. 4(c)]. Hence, the structure of the downstream wake depends on D_x. The characteristics of the three patterns are summarized in Table I.

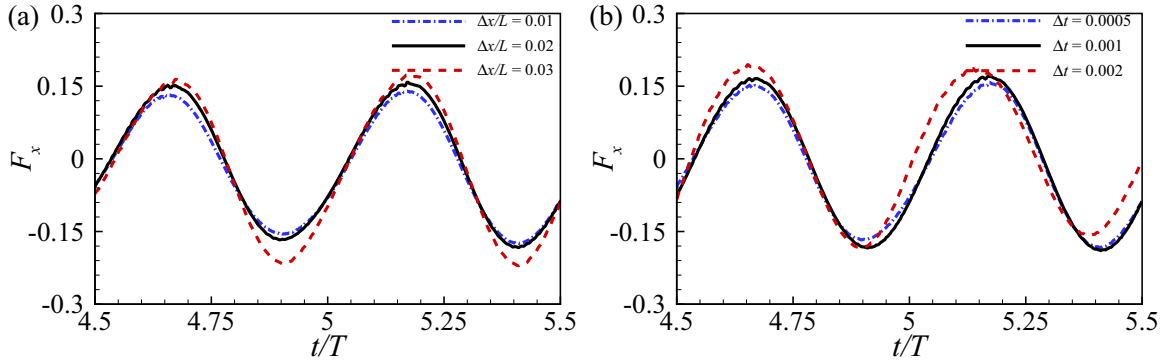

FIG. 3. The grid independence (a) and time step independence (b) studies for the case of a flexible plate flapping behind the wake of two tandem cylinders ($D_x = 1.1$, $G_0 = 10$, $A = 0.3$, $f = 0.185$, $K = 0.5$, and Re = 200). The streamwise force experienced by the plate as a function of time is presented.

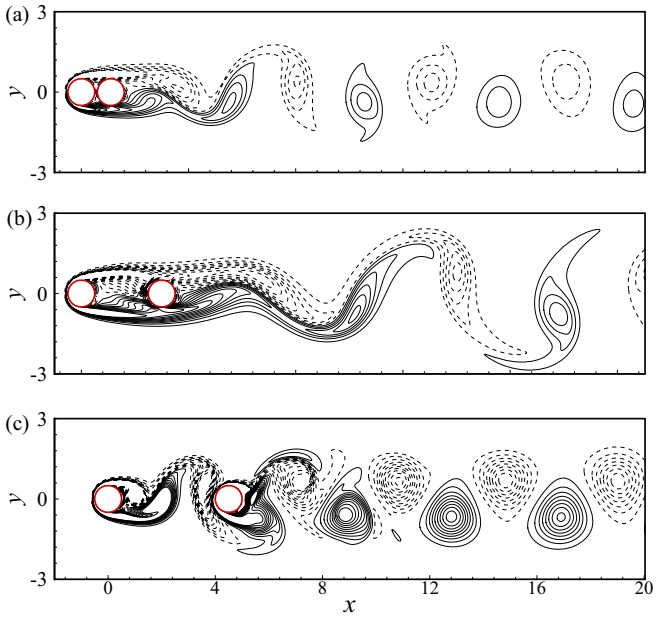

FIG. 4. Vorticity contours. (a) SBB pattern ($D_x = 1.1$), (b) SLR pattern ($D_x = 3.0$), and (c) SVS pattern ($D_x = 4.5$).

B. Self-propelled plate in the wake of cylinders

To initiate a better understanding of how fishes refuge in more complex hydrodynamic environments, here we present typical results on the locomotion of a self-propelled flexible plate in the wake of two tandem cylinders. The settings of all governing parameters are shown in Table II.

Park *et al*. [21] have shown that if the plate is able to hold stationary in the wake, the flapping frequency should be identical to that of the shedding vortices. Our numerical tests also confirmed this point. Hence, the flapping frequency of the plate is set to be the vortex shedding frequency to achieve the Kármán gait.

Wing or fin flexibility may dramatically affect the performance of flying and swimming animals [40,41]. Moore [40] developed a theory to shed new light on how flexibility can aid performance, the importance of resonance, and the separate roles played by wing and fluid inertia. Yeh and Alexeev [42] found that the free swimming velocity is maximized when the swimmer is driven near the first natural frequency. The bending stiffness $K = 0.5$ is chosen for all simulations because it is the optimal stiffness to achieve the fast propulsion for an isolated plate [13]. When $K = 0.5$, even the plate is flapping with different frequency ($f = 0.13, 0.185, 0.2$), it is also able to achieve a large propulsive velocity. The following three parameters are variables: gap spacing between two cylinders (D_x), initial position (G_0), and flapping amplitude (A). Cases of $D_x = 1.1$, 3.0, and 4.5 represent three typical flow patterns (SBB, SLR, SVS). The corresponding vortex shedding frequencies are 0.185, 0.13, and 0.185, respectively. In addition, the self-propelled flexible plate in the wake of one cylinder is also simulated for comparison.

It is noted that in all simulations except for those in Sec. IV D, initially $U = U_\infty$ is imposed everywhere in the flow field and the plate that is located at G_0 begins heaving according to Eq. (1), but it is not allowed to move longitudinally. After the shedding vortices have fully developed, the flapping is released and the longitudinal movement is allowed. Hence, at the beginning, the unreleased flapping plate would interact with the oncoming vortical structures.

1. Self-propelled plate in the three flow patterns

In our numerical settings, the SBB pattern was first investigated. The initial configuration with $G_0 \in (3, 22)$ and $A \in (0.1, 0.9)$ were simulated. When the plate was released, the plate may go forward, backward, or approximately flap in an equilibrium position depending on the initial released position. Hence, three typical modes are identified, i.e., drift upstream (DU), drift downstream (DD), and holding stationary (HS).

The typical trajectories of the three motion modes are shown in Fig. 5(a). It is seen that in the DU mode, the plate continuously swims forward with decreasing G and finally it may collide with the cylinder. One possible reason is that the plate was too close to the cylinder and trapped in the suction region on the back side of the cylinder. The other reason is that the flapping amplitude is too large and the thrust is large enough to push it forward continuously.

In the DD mode, the plate may be not able to overcome the drag force acting on the plate and is drifted downstream (G increases) continuously until it leaves the calculation domain. The HS mode is preferred and we are particulary interested in the mode. In the mode, the plate may adjust its location through swimming upstream or downstream a little bit for a while and then linger at an equilibrium G. Figure 5(b) shows the trajectory of the leading edge in one period for the HS mode, in the longitudinal direction, the leading edge of the plate would continuously move back and forth around the equilibrium location.

Our results indicate that the occurrences of the modes of the plates depend mainly on the initial location G_0 and the flapping amplitude A. The general schematic phase diagram for the three modes in the G_0-A plane is shown in Fig. 6(a). There are several critical points G_{c1}, G_{c2}, A_{c1}, and A_{c2} defined in the figure, which determine the motion mode distribution in the G_0-A plane. In different flow patterns, the values of the critical points and the distribution will be slightly different. The critical points in the phase diagram for each flow pattern

TABLE I. Characteristics of the three wake patterns behind the two tandem cylinders. f is the frequency of the vortices.

Flow pattern	D_x	f	Vorticity	Description of the vortices
SBB	Small	0.185	Moderate	The wake looks like that of a single bluff body
SLR	Moderate	0.13	Weak	The wavelength is longer, and vortices are less organized and weaker
SVS	Large	0.185	Strong	The vortices are more compact

TABLE II. The parameters in the simulations.

Reynolds number	Re	200
Mass ratio	M	1
Stretching stiffness	S	1000
Bending stiffness	K	0.5
Flapping amplitude	A	[0.1,1]
Flapping frequency	f	0.2, 0.13, 0.185
Separation distance	D_x	1.1, 3.0, 4.5
Streamwise location	G	$[-10, 40]$
Initial location	G_0	[3,25]

TABLE III. The critical points in the phase diagram.

	G_{c1}	G_{c2}	A_{c1}	A_{c2}
SBB	3.0	7.0	0.3	0.9
SLR	5.0	5.0	0.5	1.0
SVS	6.0	6.0	0.1	0.85

are shown in Table III. It is also noticed that in our study, as shown in Table II, the initial G_0 is in the range of $G_0 \in [3, 25]$ and $A \in (0, 1)$.

From Fig. 6(a), it is seen that the DU motion occurs mainly in both the top and left regions of the G_0-A plane. The DU mode appears in the left lower region because the plate is too close to the cylinder and inside the suction region. However, the DU mode appears in the top region because for a case with a large A, there is more input energy, which is able to drive it moving forward. The DD motion mode occupies the lower right region of the G_0-A plane, in which there is a small A. When G_0 and A are moderate, the HS motion mode may occur due to the Kármán gait.

The detailed phase diagram for the SVS flow pattern is shown in Fig. 6(b). Each point in the figure represents a case we simulated. Overall the phase diagram has the feature of the schematic one [Fig. 6(a)], except that in the small band of $G_0 \in (9, 10)$ there are DU and DD modes. In other words, the plate is not able to hold stationary at $G_0 \in (9, 10)$ for the SVS pattern. When the plate is initially put in this region, the unreleased flapping plate may inhibit the instability of the velocity shear layer after the cylinder, making it impossible to form a Kármán vortex street. When the plate is released, it is not able to linger at a certain location.

To better understand the inherent mechanism for the HS mode, the vortical structures and pressure distributions around the plate are investigated in the following. A typical case with $G_0 = 10$ and $A = 0.6$ in the SBB pattern is chosen to analyze.

Figures 7 and 8 show the vorticity contours and pressure contours at four typical instants of one flapping cycle, respectively. At $t = \frac{1}{8}T$, the plate is flapping upward, from Fig. 7(a), it is seen that the negative vortex shed from the cylinders extends to the upper surface of the plate. However, there is a negative pressure behind the trailing end of the plate in Fig. 8(a), which contributes to the drag force ($F_x > 0$).

At $t = \frac{3}{8}T$, Fig. 7(b) shows that at the downstroke, the shear layer shed from the upper part of the plate intensifies the negative vortical structures. Figure 8(b) shows that the pressure below the plate is higher than that above the plate. Due to the orientation of the plate, the pressure difference may result in a large thrust force.

At $t = \frac{5}{8}T$, we can see from Fig. 7(c) that the plate is flapping downward. The positive vortex shed from the cylinders extends to the lower surface of the plate. As shown in Fig. 8(c), the pressure distribution looks symmetric as that in Fig. 8(a) along the line $y = 0$. Hence, similarly there is a maximum drag force at the moment. At $t = \frac{7}{8}T$, Fig. 7(d) shows that the shear layer shed from the lower part of the plate intensifies the positive vortical structures. The pressure distribution in Fig. 8(d) is similar to that in Fig. 8(b). Hence, we have a maximum thrust force.

In the above, a typical HS case in the SBB flow pattern is analysed. For the HS case in the other two flow patterns, the situation is similar to the above SBB case. For the case of a plate in the wake of a single cylinder, Park *et al*. [21] have shown that the leading edge of the plate displays slaloming behavior between the vortex cores around the equilibrium location in the HS mode. Here in our study, the plate's slaloming behavior is also found in the SBB, SLR, and SVS flow patterns.

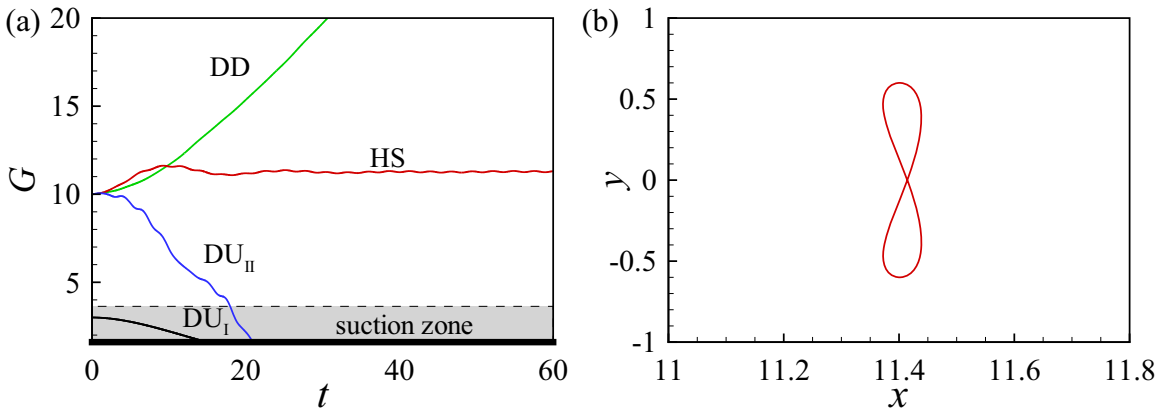

FIG. 5. (a) Streamwise trajectory of the leading edge for the three movement modes. The initial locations and flapping amplitudes are listed in the following: the DU mode (curve I) $G_0 = 3, A = 0.1$, the DU mode (curve II) $G_0 = 10, A = 0.9$, the DD mode $G_0 = 10, A = 0.1$, and the HS mode $G_0 = 10, A = 0.6$. (b) The trajectory of the leading edge in one period for the HS mode.

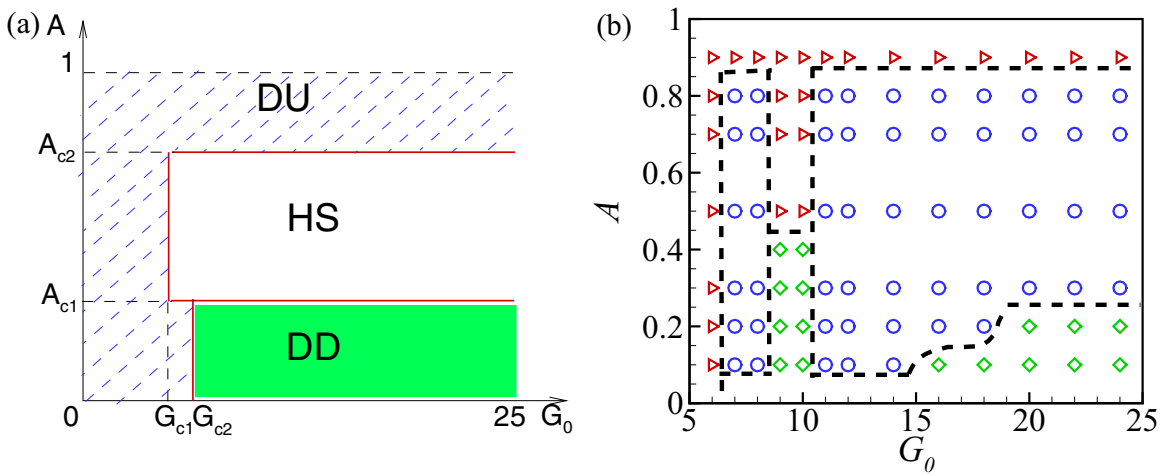

FIG. 6. (a) Schematic phase diagram for the three motion modes. Approximate critical points G_{c1}, G_{c2}, A_{c1}, and A_{c2} are able to define the motion mode distribution in the G_0-A plane. For different flow patterns, these values are listed in Table III. (b) Phase diagram for the three motion modes for SVS flow pattern. Symbols ○, ▷, and ◇ represent the HS, DU, and DD modes, respectively.

2. *The minimum A to hold stationary*

However, the stability of the HS mode may be related to the vertical flow induced by the vortices [12]. According to the vortex-dipole model, the y component of vortex-induce velocity is $V_{\Gamma,\perp} = (\Gamma/2\pi d)\sin\alpha$ [see Fig. 9(a)] [43]. In Fig. 9(b), we can see that the SLR pattern has the smallest $V_{\Gamma,\perp}$ due to the weak shedding vortices and the required minimum flapping amplitude for the HS mode is $A_{\min} \approx 0.5$. When the shedding vortices are strong, e.g., in the SVS pattern, $A_{\min} \approx 0.1$ is enough to keep the HS mode. Hence, the weaker the shedding vortices are, the larger the minimum amplitude required for the plate to keep the HS mode is.

3. *Input powers*

To further evaluate the performance of the plate in the HS mode, we quantified the input power P, which is required to actuate the leading edge of the plate. It is defined as the time average of the work done by the surface of the plate on the surrounding fluid during one flapping period T, i.e.,

$$P = \frac{1}{T}\int_{t'}^{t'+T} P(t)dt = \frac{1}{T}\int_{t'}^{t'+T}\left[\int_0^1 \boldsymbol{F}_r(s,t)\frac{\partial \boldsymbol{X}(s,t)}{\partial t}ds\right]dt, \quad (16)$$

where $\boldsymbol{F}_r$ represents the force on the surrounding fluid by the plates. The power has been calculated with an assumption that any negative contribution is ignored [44,45]. Suppose $\boldsymbol{F} = (F_x, F_y)$ is the force acting on the plate by the fluid, it is the reaction force of $\boldsymbol{F}_r$, i.e., $\boldsymbol{F} = -\boldsymbol{F}_r$. Actually, to maintain the heaving motion of the plate, the head of the plate has to be forced to oscillate up and down by an lateral external force. The work in Eq. (16) is equal to the work done by the lateral external force. Hence, the work is mainly contributed by the F_y.

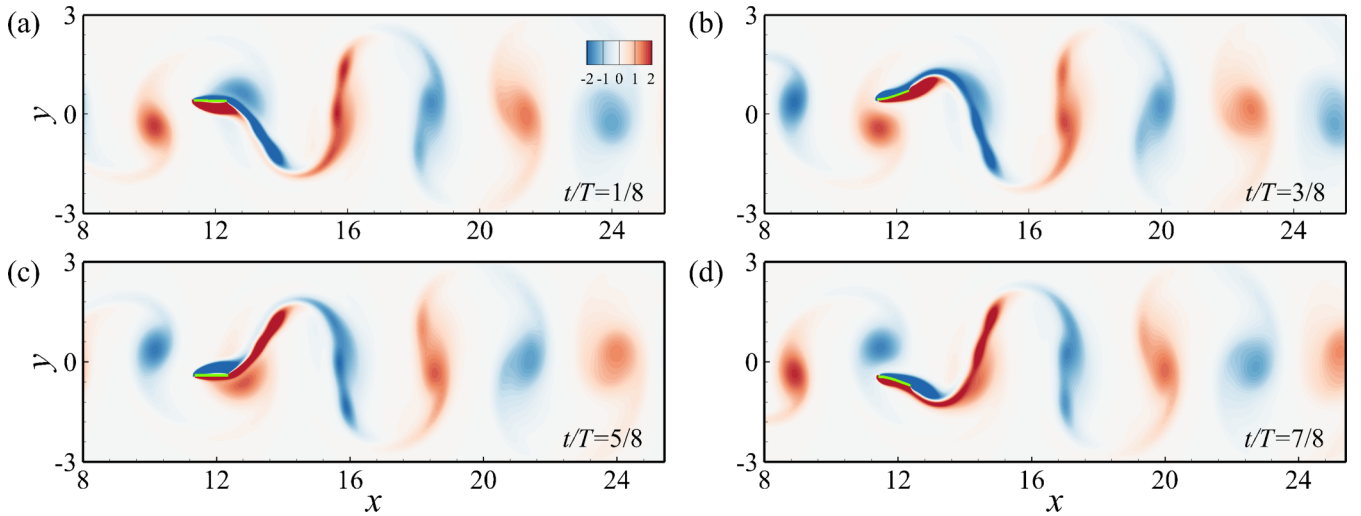

FIG. 7. Instantaneous vorticity contours at (a) $t = \frac{1}{8}T$, (b) $\frac{3}{8}T$, (c) $\frac{5}{8}T$, and (d) $\frac{7}{8}T$ in the SBB pattern. Blue and red colors denote negative and positive vorticity, respectively.

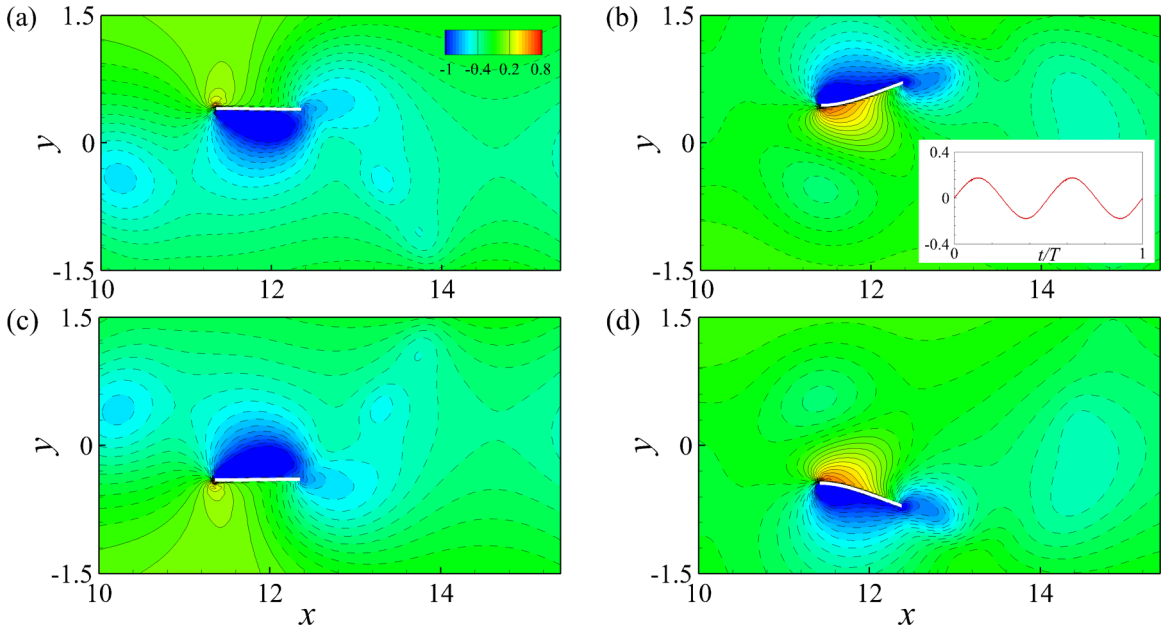

FIG. 8. Instantaneous pressure contours at (a) $t = \frac{1}{8}T$, (b) $t = \frac{3}{8}T$, (c) $t = \frac{5}{8}T$, (d) $t = \frac{7}{8}T$ in the SBB pattern ($G_0 = 10$ and $A = 0.6$). The inset in (b) represents an instantaneous longitudinal force F_x of the plate. Solid and dashed lines denote the positive and negative normalized pressure contours, respectively.

As we know, due to dissipation, the shedding vortex street becomes weak when it is far from the rear cylinder. Supposing the wake speed decays exponentially in time and using the approximation of viscous and turbulent dissipation [46,47], we have the conclusion that the wake speed oscillates and decays with downstream distance.

To make a comparison for the cases in the three different flow patterns, we have to make sure that the gap spacing is properly chosen, so that the vortex strength before the plate could represent the wake characteristics of the flow pattern. We found that $G_0 \approx 10$, 12, and 14 for the SBB ($D_x = 1.1$), SLR ($D_x = 3.0$), and SVS ($D_x = 4.5$) flow patterns, respectively, is proper because $G_0 - D_x \approx 9$.

In this way, our comparison of quantities in different flow pattern is reasonable. The input power of the plate in the HS mode as a function of A is shown in Fig. 10(a). It is seen that the input power P in each flow pattern increases as A increases. It can be easily understood because a flapping with a larger amplitude usually requires more input energy.

It is seen that when $A < 0.5$, the corresponding P in the SVS pattern is smaller than that of the SBB. As we have seen, to hold stationary the minimum flapping amplitude A in the SVS is only about 0.1. Hence, to achieve the HS mode, the plate in the SVS wake pattern could get more hydrodynamic advantage and therefore consumes the least input power when $A < 0.5$.

When $A > 0.5$, the plate in the SVS wake pattern still consumes less input power than that in the SBB, because the SVS pattern has a smaller F_y amplitude than the SBB pattern when $A = 0.6$ [see Fig. 10(b)]. It is noticed in Fig. 10(b), $T = \frac{1}{f}$ of the SLR is larger than those of the SBB and SVS patterns (see Table I). It is also seen that when $A > 0.5$, the corresponding P in the SLR pattern is usually the smallest among the three patterns. It can be understood as follows. The vortex shedding frequency of the SLR pattern is significantly smaller than

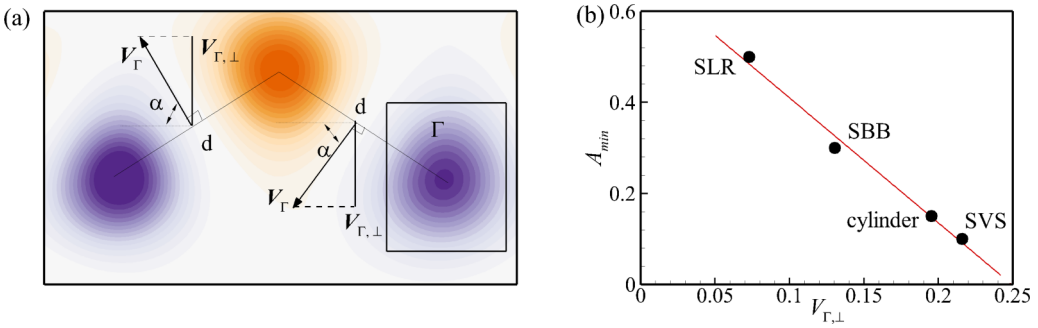

FIG. 9. (a) The schematic diagram of the vortex-induced velocity. (b) The minimum amplitude required for the HS mode in the three flow patterns as a function of y component of vortex-induced velocity $V_{\Gamma,\perp}$ (the case in the wake behind a single cylinder is also shown). Here, α is the orientation angle between the dipole-induced velocity V_Γ and the x axis, d is the distance between two vortex centers, and Γ is the circulation of the vortex.

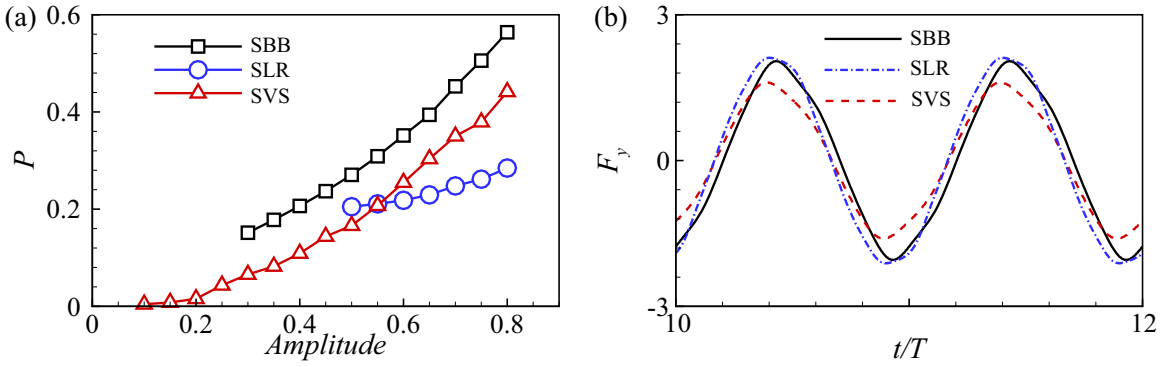

FIG. 10. (a) Input power P as functions of A; (b) vertical force experienced by the plate ($A = 0.6$) as functions of times, where the black, blue and red lines represent the SBB, SLR, and SVS flow patterns, respectively. It is noted that $T = \frac{1}{f}$ of the SLR is larger than those of the SBB and SVS patterns (see Table I).

those of the SBB and SVS patterns. Hence, the plate's flapping frequency in the SLR pattern is the smallest among the three patterns, which requires the least y-component velocity v_y when flapping. Although the difference of the F_y amplitude in the three patterns is not significant when $A = 0.6$ [see Fig. 10(b)], because $P \approx \frac{1}{T}\int_{t'}^{t'+T} F_y v_y dt$, the SLR needs the least input power.

C. Equilibrium mechanism

Figure 11 shows the effect of the initial location of the plate on the equilibrium location. We can see that except for two cases in Fig. 11(c), when the plate is released at different initial location G_0, it will go back and forth for a while and then it would linger at a certain equilibrium location, with a small oscillating amplitude.

In the SBB flow pattern [see Fig. 11(a)], after $t > 20$, in each case the plate almost reaches an equilibrium location. For a initial location $G_0 \in (3, 16)$, there are four discrete equilibrium locations, i.e., $G^{\text{eq}} \approx 4.5$, 7.5, 11.0, and 14.5. The gap spacings between neighboring discrete equilibrium locations are approximately 3, while the corresponding wavelength of the wake is about 5.

In the SLR flow pattern [see Fig. 11(b)], it is seen that in the 9 cases, when $t > 40$, each plate almost reaches an equilibrium location. The discrete equilibrium locations are $G^{\text{eq}} \approx 9.5$, 16.0, and 22.0. The gap spacings between neighboring discrete equilibrium locations are approximately 6, and the corresponding wavelength of the wake is about 6. In the SVS flow pattern [see Fig. 11(c)], the equilibrium locations are much more scattered than those in the SBB and SLR patterns. The equilibrium locations seem very close to the corresponding initial locations. It is also seen that when $G_0 \in (9, 10)$, the plate is drift forward and not able to hold stationary [see the discussion on Fig. 6(b)].

Previous studies also observed that there are several equilibrium locations in the vortical wakes. Ramananarivo *et al.* [12] and Peng *et al.* [13] have presented explanations. They found that the hydrodynamic force near G^{eq} is a springlike restoring force with $F_x = -k(G - G_i^{\text{eq}})$, where G_i^{eq} is the ith stable equilibrium location with a positive k, which is analogous to the spring constant. When the initial location of the plate is located close to an equilibrium point, it may finally linger at the equilibrium point where $F_x = 0$.

Numerical simulations were performed to calculate the hydrodynamic forces on the plate [12,48]. In these simulations,

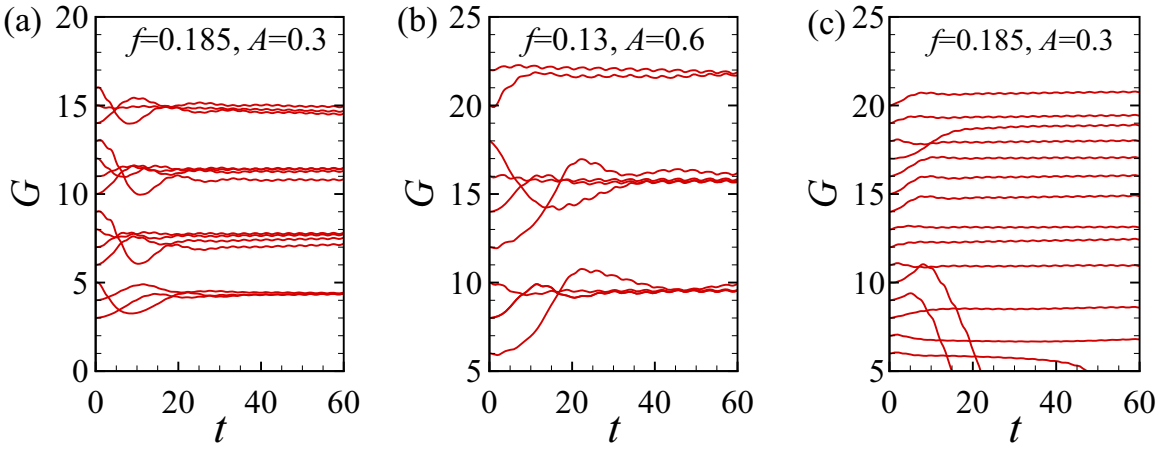

FIG. 11. Streamwise trajectories of the leading edge in cases with different G_0 for the (a) SBB pattern, (b) SLR pattern, and (c) SVS pattern. Each curve represents a case we simulated.

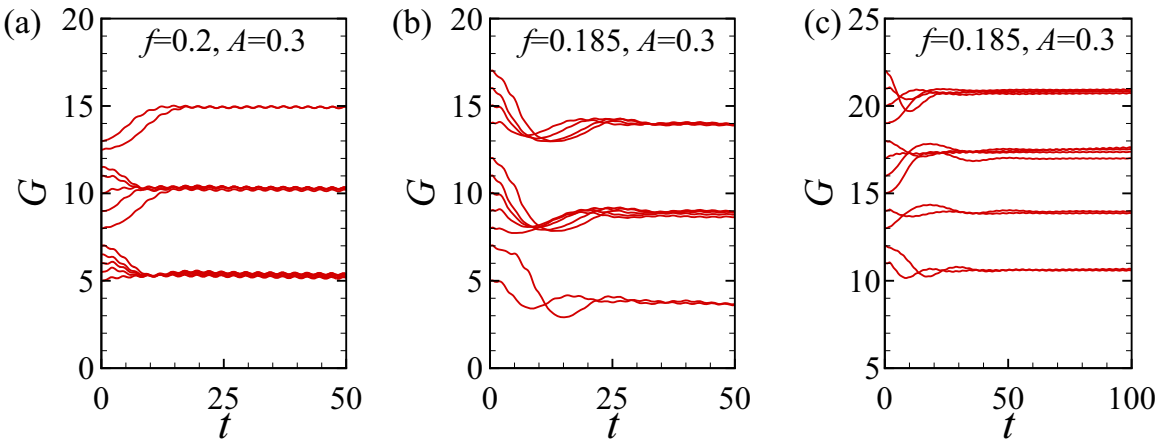

FIG. 12. Streamwise location of the leading edge as a function of time for cases with different G_0. In the cases, the releasing style in Ref. [21] was adopted. (a) The plate is self-propulsive behind a single cylinder. The key parameters Re, M, K, A, f are identical to those in Ref. [21]. (b) The plate is self-propulsive in the SBB pattern and (c) the SVS pattern of two tandem cylinders.

the plate is only flapping up and down and its longitudinal location is fixed. In all of the three flow patterns, we observed that the net horizontal force F_x acting on the plate as a function of G_0 is similar to those in Refs. [12,13], i.e., F_x near G^{eq} is a springlike restoring force (not shown).

Actually the releasing style may play a more important role in the mechanism of the HS mode. In the following, we will discuss this issue.

D. Releasing style

According to the study of Park *et al*. [21], when the self-propelled flexible plate is behind the wake of a circular cylinder, the gap spacing between neighboring discrete equilibrium positions ζ is equal to the wake wavelength λ. Since the SBB flow pattern is similar to the wake flow of the single cylinder, it is expected that the corresponding ζ should be equal to λ of the SBB pattern. However, in our SBB result, $\zeta \approx 3.0 = 0.6\lambda$, where $\lambda \approx 5.0$. Our result is different from that in Park *et al*. [21].

We conjectured that the releasing style may contribute to this difference. It is noticed that in the study of Park *et al*. [21] the plate was initially kept stationary and began to flap once the vortical structures were fully developed, which is different from our present releasing style mentioned in Sec. IV B. In the following descriptions, our releasing style is referred to as Style I, and that in Park *et al*. [21] is Style II.

To confirm our conjecture, in this section the releasing Style II is adopted in our simulations. The streamwise trajectories of the self-propelled flexible plate in the wake of a single cylinder, SBB pattern and SVS pattern of two tandem cylinders are presented in Fig. 12 (The streamwise trajectories of SLR pattern of two tandem cylinders is similar to that in the releasing Style I.) It is seen that for one cylinder pattern and the SBB pattern, the gap spacing between neighboring discrete G^{eq} is approximately 5 [see Figs. 12(a) and 12(b)], which is close to the λ in the wake. For SVS pattern, G^{eq} is approximately 3.5 ($\lambda \approx 4$) [see Fig. 12(c)], which is different from that in Style I. Hence, by changing the releasing style, we successfully reproduced the result in Park *et al*. [21]. Besides, we found that the releasing style indeed affects the flow field much.

To explore how our releasing style affects the flow field, four cases of the flexible plate in the wake of a single cylinder with different releasing styles were simulated. For the releasing Style II, we chose two cases with $G_0 = 9$ and 14, the initial gap spacing between them is approximately equal to one wavelength of the shedding vortices ($\lambda \approx 5$). The instantaneous vorticity fields at the moment when the plate is released are shown in Fig. 13. In Figs. 13(a) and 13(b), the releasing Style II [21] is applied. It is seen that at $t = 0$, phases of vortex shedding in the two cases of $G_0 = 9$ and 14 are identical. They are also consistent with the case without the plate [see the inset in Fig. 13(a)]. Hence, the releasing Style II almost does not affect the vortex shedding of the cylinder. Besides, the vortical flows around the two plates are identical. After the plates are released, the flapping of the two plates are also inphase. Hence, their locomotion and the surrounding flows should be fully synchronized. We can imagine that the gap spacing between the two plates in Figs. 13(a) and 13(b) should always be equal to the initial gap spacing λ during the dynamic evolution until they reach their equilibrium locations with $\zeta \approx \lambda = 5$.

In Figs. 13(c) and 13(d), the releasing Style I is applied. It is seen that phases of vortex shedding in the two cases of $G_0 = 9$ and 12 at $t = 0$ are different and not inphase. Hence, compared to the releasing Style II, the releasing Style I seems able to change the phase of vortex shedding significantly. It is due to the fact that the plate is continuously flapping at G_0 before the releasing moment ($t = 0$). It is noticed that the simulations were performed from $t = -20T$. However, the vortical flows around the two plates are identical in Figs. 13(c) and 13(d). At the moment, the flapping of the two plates is also inphase. Hence, the gap spacing between the two plates in Figs. 13(c) and 13(d) should also be equal to the gap spacing at $t = 0$ during the dynamic evolution until they reach their equilibrium locations with $\zeta = 3 \approx 0.6\lambda$.

Hence, when the plate is released in Style I due to the smaller ζ, it is able to achieve more equilibrium locations in the same wake region compared to the situation of Style II.

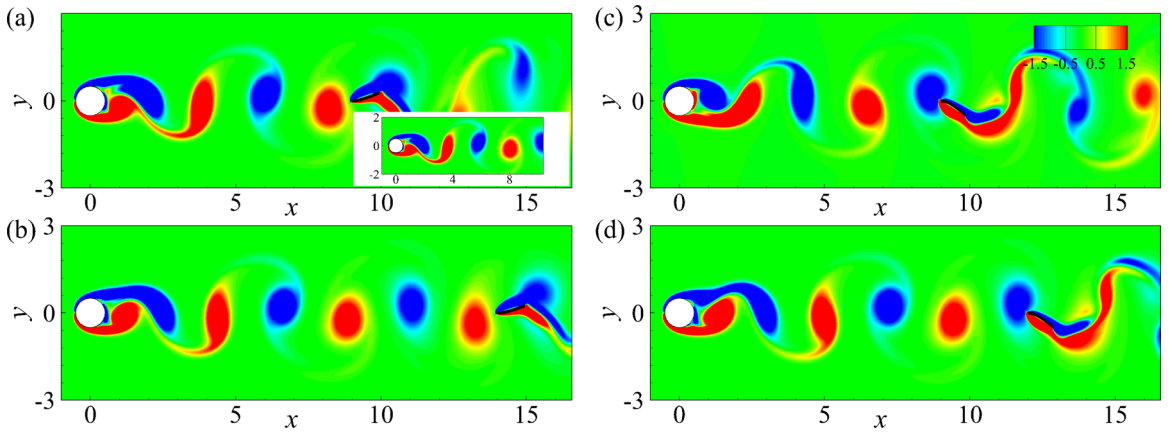

FIG. 13. Instantaneous vorticity contours at the releasing moment for four cases with different releasing styles, (a) the case of $G_0 = 9$ with releasing Style II [21], (b) the case of $G_0 = 14$ with releasing Style II, (c) the case of $G_0 = 9$ with releasing Style I, (d) the case of $G_0 = 12$ with releasing Style I. The inset in (a) represents an instantaneous vorticity contour without the plate. Blue and red colors denote negative and positive vorticity, respectively.

The inherent mechanism is that the phase of vortex shedding behind the cylinder can be changed in Style I due to the continuously flapping before the releasing. Changing the phase of vortex shedding is favorable because the plate becomes easier to hold stationary. It seems that in Style I, the effort of the pre-flapping is not in vain because although it consumes more energy, it could hold stationary quickly in the longitudinal direction after it is released. The Kármán gait becomes easier.

For the real fish, it may adopt a strategy like Style I. Stewart *et al*. [26] have mentioned that Trout Kármán gait is able to hold stationary anywhere in a certain area behind the *D*-shaped cylinder, not a few discrete equilibrium locations, because the fish can adjust the gait timely according to different flow condition. It is believed that if the fish changes the flapping amplitude and phase in Style I, it may be able to hold stationary at its initial location by adjusting the phase of vortex shedding. Hence, our releasing style (Style I) is more consistent with the real situation.

To quantify the effect of the two releasing styles, we took the strategy of Son and Choi, [49] and measured the vertical velocities (v) as functions of time at certain centerline locations in the wake to describe the phase of vortex shedding quantitatively. Specifically, the locations are chosen to be $(x, y) = (6, 0)$ and $(G_0 - 0.5, 0)$. The first point is behind the cylinder and the second point is just in front of the plate (see Fig. 14).

We suppose that the phase at point (6, 0) for the case $G_0 = 9$ at the releasing moment ($t = 0$) is zero (the simulations started at $t = -30T$). In Style II, the time histories of v at (6, 0) in the cases with different G_0 have identical phase of vortex shedding [see Figs. 13(a) and 13(b), and the red triangles in Fig. 14(a)]. It seems that in Style II, the stationary flapping plate does not affect the vortex shedding. In this way, the vortex shedding phase that the plate faces is only determined by G_0. When G_0 increases 1, there is a $\frac{1}{5}T$ phase advance at $(G_0 - 0.5, 0)$. Hence, the points $G_0 = 9$ and 14 have the same phase (see Fig. 13).

However, in Style I [see Fig. 14(b)], when G_0 increases from $G_0 = 9$ to 10, the phase of vortex shedding advances $\frac{2}{15}T$ at (6, 0) (see the red triangles). At $(G_0 - 0.5, 0)$, the phase of v advances $\frac{1}{3}T$ when G_0 increases 1. In other words, the phases in front of the plate in the cases of $G_0 = 9$ and 12 are identical

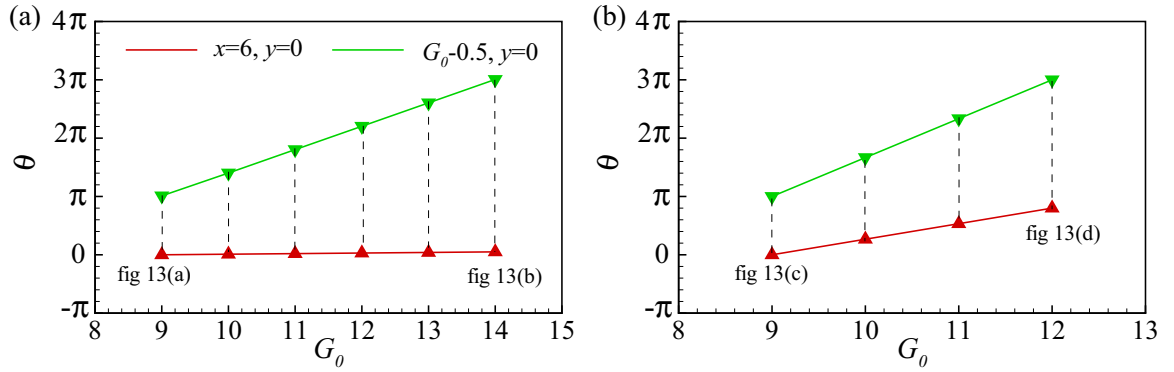

FIG. 14. The phases of v at the releasing moment ($t/T = 0$) for fixed points with different releasing styles, (a) the phase at (6, 0) and $(G_0 - 0.5, 0)$ with releasing Style II, (b) the phase at (6, 0) and $(G_0 - 0.5, 0)$ with releasing Style I, respectively. Every two points in a vertical dashed line represents a case we simulated.

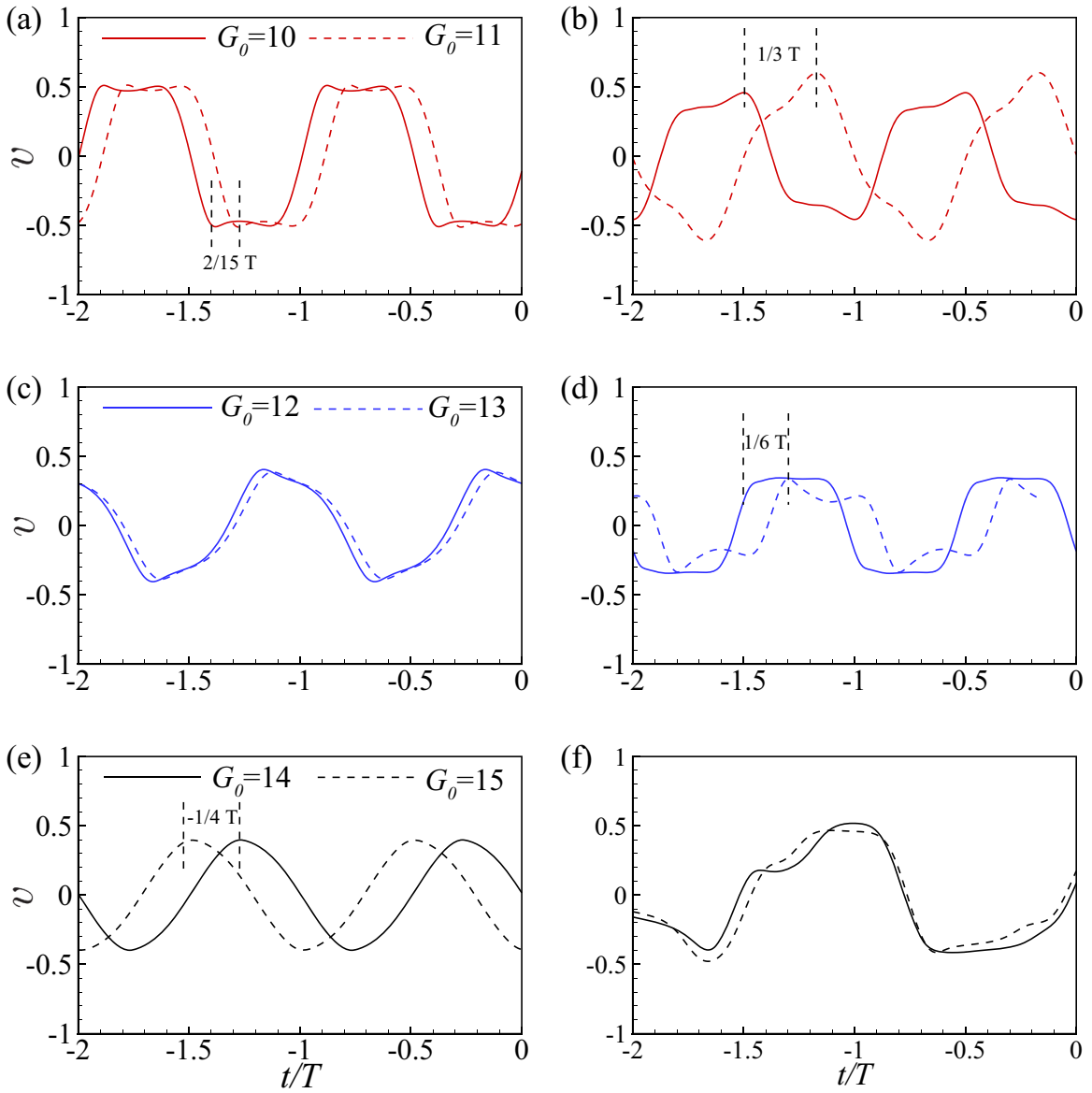

FIG. 15. Instantaneous vertical velocity v before the releasing moment ($t/T = 0$) at fixed points (releasing Style I). The left and right columns represent the time history of v at (6,0), and ($G_0 - 0.5$,0), respectively. The upper, middle, and lower rows represent cases in the SBB, SLR, and SVS wake patterns, respectively. For all cases, $A = 0.6$.

(see the green triangles). So we can conclude that the phase of v in front of the plate is determined by the phase of vortex shedding behind the cylinder and G_0.

From the above analyses, we conjectured that the gap spacing between neighboring discrete equilibrium locations ζ depends on the wake wavelength λ, the increase of ΔG_0, and the corresponding time lag $\Delta\theta$. Here, a formula including these factors are proposed to calculate ζ,

$$\zeta = \frac{2\pi}{\frac{\Delta\theta}{\Delta G_0} + \frac{2\pi}{\lambda}}, \tag{17}$$

where $\Delta G_0 < \zeta$.

Although the formula is proposed from the flow pattern of a single cylinder in Style I, we would like to check whether Eq. (17) is applicable to flow patterns of two cylinders.

For the SBB pattern, time histories of v at locations (6, 0) and $(G_0 - 0.5, 0)$ are shown in Figs. 15(a) and 15(b) for two cases with $G_0 = 10$ and 11. At (6, 0), the phase of the case $G_0 = 11$ advances $\frac{2}{15}T$, i.e., $\frac{4}{15}\pi$ compared to the case of $G_0 = 10$ [see the dashed red line in Fig. 15(a)]. Hence, $\zeta = \frac{2\pi}{\frac{4/15\pi}{1} + \frac{2\pi}{5}} = 3$. As a result, for the phase of v in front of the plate, there is a time advance of $\frac{T}{3}$ [see Fig. 15(b)].

For the SLR pattern, time histories of v at locations (6, 0) and $(G_0 - 0.5, 0)$ are shown in Figs. 15(c) and 15(d) for two cases with $G_0 = 12$ and 13. It is seen that at (6, 0) the vortex shedding of the two cases is inphase. The possible reason is that the vortices are too weak and the releasing Style I is not able to change the vortex shedding phase. Using the formula, we get $\zeta = \frac{2\pi}{0 + \frac{2\pi}{6}} = 6 \approx \lambda$. As a result, in front of the plate, there is a time advance of $\frac{1}{6}T$ for the two cases with $\Delta G_0 = 1$.

For the SVS pattern [see Figs. 15(e) and 15(f)], there is a time lag $\frac{1}{4}T$ when G_0 increases 1, i.e., $\Delta\theta = -\frac{1}{2}\pi$. In the pattern, the wake wavelength $\lambda \approx 4$. Using the formula, we get $\zeta = \infty$. So the vortical flows in front of the two plates are identical [see Fig. 15(f)]. Therefore, the equilibrium locations are very close to the corresponding initial locations. In other words, the SVS pattern could hold stationary at any location to some extent.

The above results of ζ coincide with those in Fig. 11. Hence, Eq. (17) is valid for all three flow patterns. The possible mechanism is that in the incompressible flow field, the releasing Style I is able to adjust the vortex shedding behind the cylinders in advance, and make it favorable for the plate to reach the HS state. However, the adjustment ability of the releasing Style II is limited because the vortex shedding has been fully developed when it is released.

V. CONCLUDING REMARKS

The self-propelled flexible plate in the wake of two tandem cylinders was investigated numerically. Adjusting the gap spacing D_x of the cylinders, the SBB, SLR, and SVS flow patterns would appear. Three typical locomotion modes of the plate, i.e., the DU, DD, and HS modes, have been identified. The mode distribution in the G_0-A plane is presented. It is found that usually when G_0 and A are moderate, the HS mode may occur due to the Kármán gait.

The interaction between the shedding vortical structure and the plate helps the plate to hold stationary in the wake patterns. Generally speaking, in the SBB, SLR, and SVS patterns, stronger vortices may induce larger y-component velocity, which is helpful to decrease the minimum amplitude required for the plate to hold stationary at an equilibrium location. We also found that to achieve the HS mode, the plate in the SVS wake pattern consumes the least input power. The consumed input power P of the plate in the three motion modes all increases as A increases.

The influence of different releasing styles was discussed. For different G_0, in Style II the flapping plate has a very minor effect on the shedding vortices. The gap spacing between neighboring G^{eq} is approximately equal to λ. When the plate is released in Style I, we found that it is able to achieve more equilibrium locations in the same wake region compared to the situation of Style II. The inherent mechanism is that the continuously flapping before the releasing may change the phase of vortex shedding behind the cylinder in Style I. In this way the plate becomes easier to hold stationary.

Finally, we measured the vertical velocity at a centerline location in the wake as a sensing variable to quantify the phase of vortex shedding behind the cylinder. Furthermore, Eq. (17) using the time (lag or advance) information is proposed, which is able to predict the gap spacing between neighboring G^{eq}. The formula is validated in all three flow patterns.

In our study, the simulations were limited to 2D cases to save computational resources. Actually, our study is a model study instead of the cases in reality. However, our 2D self-propelled model is reasonable and it may scrap enough physics. In our 2D flapping plate model, the head of the plate is flapping and the other part of the plate passively deforms due to the fluid-structure interaction. The character is consistent with the observation of Liao *et al*. [22], i.e., when trout adopts the Kármán gait, it only activates their anterior axial muscles, act as a self-correcting hydrofoil. However, our 2D cases may share some common mechanisms with 3D cases in reality. For example, the reproduced Kármán gait in the 2D simulation [21] is similar to that in the 3D experiment [22,50]. Hence, the 2D study may reveal mechanisms of the fluid-structure interaction problem.

There are some limitations in our study, such as the simple actuation of the swimming and Reynolds number is not high. Anyway, the present study may shed some light on a better understanding of hydrodynamic effect on fish refuging in complex hydrodynamic environments.

ACKNOWLEDGMENTS

This work was supported by the Natural Science Foundation of China (NSFC) Grants No. 11872064 and No. 11621202. H.H. is supported by NSFC Grants No. 11972342 and No. 11772326.

[1] D. H. Cushing and F. R. H. Jones, Why do fish school? Nature **218**, 918 (1968).
[2] B. L. Partridge and T. J. Pitcher, Evidence against a hydrodynamic function for fish schools, Nature **279**, 418 (1979).
[3] D. Weihs, Hydromechanics of fish schooling, Nature **241**, 290 (1973).
[4] D. Weihs, *Some Hydrodynamical Aspects of Fish Schooling* (Springer, Berlin, 1975).
[5] C. K. Hemelrijk, D. A. P. Reid, H. Hildenbrandt, and J. T. Padding, The increased efficiency of fish swimming in a school, Fish Fisheries **16**, 511 (2015).
[6] I. Ashraf, H. Bradshaw, T.-T. Ha, J. Halloy, R. Godoy-Diana, and B. Thiria, Simple phalanx pattern leads to energy saving in cohesive fish schooling, Proc. Natl. Acad. Sci. USA **114**, 9599 (2017).
[7] M. V. Abrahams and P. W. Colgan, Fish schools and their hydrodynamic function: A reanalysis, Environ. Biol. Fish. **20**, 79 (1987).
[8] S. S. Killen, S. Marras, J. F. Steffensen, and D. J. McKenzie, Aerobic capacity influences the spatial position of individuals within fish schools, Proc. R. Soc. B **279**, 357 (2012).
[9] S. J. Portugal, T. Y. Hubel, J. Fritz, S. Heese, D. Trobe, B. Voelkl, S. Hailes, A. M. Wilson, and J. R. Usherwood, Upwash exploitation and downwash avoidance by flap phasing in ibis formation flight, Nature **505**, 399 (2014).
[10] S. Alben, On the swimming of a flexible body in a vortex street, J. Fluid Mech. **635**, 27 (2009).
[11] X. J. Zhu, G. W. He, and X. Zhang, Flow-Mediated Interactions Between Two Self-Propelled Flapping Filaments in Tandem Configuration, Phys. Rev. Lett. **113**, 238105 (2014).

[12] S. Ramananarivo, F. Fang, A. Oza, J. Zhang, and L. Ristroph, Flow interactions lead to orderly formations of flapping wings in forward flight, Phys. Rev. Fluids **1**, 071201 (2016).

[13] Z.-R. Peng, H. Huang, and X.-Y. Lu, Collective locomotion of two self-propelled flapping plates with different propulsive capacities, Phys. Fluids **30**, 111901 (2018).

[14] J. Heggenes, Effects of short-term flow fluctuations on displacement of, and habitat use by, brown trout in a small stream, Trans. Am. Fish. Soc. **117**, 336 (1988).

[15] P. W. Webb, The effect of solid and porous channel walls on steady swimming of steelhead trout *Oncorhynchus mykiss*, J. Exp. Biol. **178**, 97 (1993).

[16] P. W. Webb, Entrainment by river chub *Nocomis micropogon* and smallmouth bass *Micropterus dolomieu* on cylinders, J. Exp. Biol. **201**, 2403 (1998).

[17] J. D. Eldredge and D. Pisani, Passive locomotion of a simple articulated fish-like system in the wake of an obstacle, J. Fluid Mech. **607**, 279 (2008).

[18] L.-B. Jia and X.-Z. Yin, Response modes of a flexible filament in the wake of a cylinder in a flowing soap film, Phys. Fluids **21**, 101704 (2009).

[19] X. M. Shao, D. Y. Pan, J. Deng, and Z. S. Yu, Hydrodynamic performance of a fishlike undulating foil in the wake of a cylinder, Phys. Fluids **22**, 111903 (2010).

[20] F.-B. Tian, H. Luo, L. Zhu, and X.-Y. Lu, Interaction between a flexible filament and a downstream rigid body, Phys. Rev. E **82**, 026301 (2010).

[21] S. G. Park, B. Kim, and H. J. Sung, Self-propelled flexible fin in the wake of a circular cylinder, Phys. Fluids **28**, 111902 (2016).

[22] J. C. Liao, D. N. Beal, G. V. Lauder, and M. S. Triantafyllou, The Kármán gait: Novel body kinematics of rainbow trout swimming in a vortex street, J. Exp. Biol. **206**, 1059 (2003).

[23] J. C. Liao, Neuromuscular control of trout swimming in a vortex street: Implications for energy economy during the Karman gait, J. Exp. Biol. **207**, 3495 (2004).

[24] M. Taguchi and J. C. Liao, Rainbow trout consume less oxygen in turbulence: The energetics of swimming behaviors at different speeds, J. Exp. Biol. **214**, 1428 (2011).

[25] D. N. Beal, F. S. Hover, M. S. Triantafyllou, J. C. Liao, and G. V. Lauder, Passive propulsion in vortex wakes, J. Fluid Mech. **549**, 385 (2006).

[26] W. J. Stewart, F.-B. Tian, O. Akanyeti, C. J. Walker, and J. C. Liao, Refuging rainbow trout selectively exploit flows behind tandem cylinders, J. Exp. Biol. **219**, 2182 (2016).

[27] S. Michelin and S. G. Llewellyn Smith, Resonance and propulsion performance of a heaving flexible wing, Phys. Fluids **21**, 071902 (2009).

[28] B. S. H. Connell and D. K. P. Yue, Flapping dynamics of a flag in a uniform stream, J. Fluid Mech. **581**, 33 (2007).

[29] S. Y. Chen and G. D. Doolen, Lattice Boltzmann method for fluid flows, Annu. Rev. Fluid Mech. **30**, 329 (1998).

[30] J. F. Doyle, *Nonlinear Analysis of Thin-walled Structures: Statics, Dynamics, and Stability* (Springer, Berlin, 2001).

[31] C. S. Peskin, The immersed boundary method, Acta Numer. **11**, 479 (2002).

[32] R. Mittal and G. Iaccarino, Immersed boundary methods, Annu. Rev. Fluid Mech. **37**, 239 (2005).

[33] Z. Guo, C. Zheng, and B. Shi, Discrete lattice effects on the forcing term in the lattice Boltzmann method, Phys. Rev. E **65**, 046308 (2002).

[34] Z.-R. Peng, H. Huang, and X.-Y. Lu, Hydrodynamic schooling of multiple self-propelled flapping plates, J. Fluid Mech. **853**, 587 (2018).

[35] Z.-R. Peng, H. Huang, and X.-Y. Lu, Collective locomotion of two closely spaced self-propelled flapping plates, J. Fluid Mech. **849**, 1068 (2018).

[36] C. Tang, H. Huang, P. Gao, and X.-Y. Lu, Self-propulsion of a flapping flexible plate near the ground, Phys. Rev. E **94**, 033113 (2016).

[37] T. Igarashi, Characteristics of the flow around two circular cylinders arranged in tandem: 1st report, Bull. JSME **24**, 323 (1981).

[38] D. Sumner, S. J. Price, and M. P. Paidoussis, Flow-pattern identification for two staggered circular cylinders in cross-flow, J. Fluid Mech. **411**, 263 (2000).

[39] S. Y. Wang, F. B. Tian, L. B. Jia, X.-Y. Lu, and X.-Z. Yin, Secondary vortex street in the wake of two tandem circular cylinders at low Reynolds number, Phys. Rev. E **81**, 036305 (2010).

[40] M. N. J. Moore, Analytical results on the role of flexibility in flapping propulsion, J. Fluid Mech. **757**, 599 (2014).

[41] R.-N. Hua, L. Zhu, and X.-Y. Lu, Locomotion of a flapping flexible plate, Phys. Fluids **25**, 121901 (2013).

[42] P. D. Yeh and A. Alexeev, Free swimming of an elastic plate plunging at low Reynolds number, Phys. Fluids **26**, 053604 (2014).

[43] R. Godoy-Diana, C. Marais, J.-L. Aider, and J.-E. Wesfreid, A model for the symmetry breaking of the reverse Bénard–von Kármán vortex street produced by a flapping foil, J. Fluid Mech. **622**, 23 (2009).

[44] N. Arora, C.-K. Kang, W. Shyy, and A. Gupta, Analysis of passive flexion in propelling a plunging plate using a torsion spring model, J. Fluid Mech. **857**, 562 (2018).

[45] B. Yin and H. Luo, Effect of wing inertia on hovering performance of flexible flapping wings, Phys. Fluids **22**, 111902 (2010).

[46] J. W. Newbolt, J. Zhang, and L. Ristroph, Flow interactions between uncoordinated flapping swimmers give rise to group cohesion, Proc. Natl. Acad. Sci. USA **116**, 2419 (2019).

[47] A. D. Becker, H. Masoud, J. W. Newbolt, M. Shelley, and L. Ristroph, Hydrodynamic schooling of flapping swimmers, Nat. Commun. **6**, 8514 (2015).

[48] T. Y. Wu and A. T. Chwang, *Extraction of Flow Energy by Fish and Birds in a Wavy Stream* (Springer, Berlin, 1975).

[49] D. Son and H. Choi, Iterative feedback tuning of the proportional-integral-differential control of flow over a circular cylinder, IEEE Trans. Control. Syst. Technol. **27**, 1385 (2018).

[50] J. C. Liao, D. N. Beal, G. V. Lauder, and M. S. Triantafyllou, Fish exploiting vortices decrease muscle activity, Science **302**, 1566 (2003).